

**RICE UNIVERSITY**

**Characterization of Antimonide-Based Compound  
Semiconductors and Quantum Wire Fabrication**

**by**

**Shanna Crankshaw**

A THESIS SUBMITTED IN  
PARTIAL FULFILLMENT OF THE  
REQUIREMENTS FOR THE DEGREE

**Bachelor of Science**

HOUSTON, TEXAS

April 25, 2003

## Abstract

### **Characterization of Antimonide-Based Compound Semiconductors and Quantum Wire Fabrication**

by

Shanna Crankshaw

Quantum confinement of bulk systems will often reveal novel behaviors unseen in the classical regime. This study investigates the magneto-transport properties of antimonide-based compound semiconductors (ABCS) in such a reduced-dimensional scheme. This 6.1-Å family of III-V semiconductors includes InAs and AlSb, whose large conduction band offset affords great flexibility in their bandgap engineering. The samples under investigation consist of a twenty-period InAs/AlSb superlattice on a GaAs substrate. A 10 Tesla superconducting magnet, operating at liquid  $^4\text{He}$  temperatures, is used to determine the electronic transport properties of the two-dimensional electron gas (2DEG) confined in the InAs layers. The theoretical motivations and experimental results of these measurements will be presented in detail. In order to further investigate the effects of quantum confinement on transport properties, electron-beam lithography is used to fabricate split Schottky gates on the heterostructure surface, with an additional layer of silicon oxide insulation deposited to minimize gate leakage. The elements and considerations in this fabrication process will also be explained. Applying a negative voltage to the lithographically defined gates creates an electrostatically tunable one-dimensional constriction in the underlying superlattice, ideally suited for further studies in electronic and spin transport.

## Acknowledgements

My thanks go first to my research advisor, Prof. Jun Kono, for all of his academic support and, of course, technical expertise, in this project. When I began attending, nearly two years ago, the graduate seminar that he was teaching at the time, I certainly could not have told anyone the difference between a heavy hole or a light hole, or how an exciton can Bose condense—or even what an exciton was for that matter. I owe much of my interest in semiconductors, in nanostructures, and, not surprisingly, in semiconductor nanostructures to that early exposure of topics which so often had the effect of my thinking, “neat,” without understanding what was going on that it proved a rather strong impetus for pursuing other courses in solid-state physics and electronics. I must also thank Dr. Giti Khodaparast and Diane Larrabee for helping in the lab this year, and doing things like tempering potentially tedious hours of pumping and flushing the magnet system with trips to the Istanbul Grill. Sasa Zaric also deserves mention for his help last year especially, expending hours of initial training time on the SEM with me, and in the waiting time for the machine to stabilize or the evaporator to pump down giving me the rudiments of an education in this pop culture thing that I hear of from time to time. Truly, I owe my appreciation to all of the graduate students in this group—Gordana Ostojic, Jigang Wang, Ajit Srivastava—for their help and discussions. I must also recognize the collaboration with the Osaka Institute of Technology, with Profs. Masataka Inoue and Shigehiko Sasa, for providing the many ABCS samples used in this project. Additionally, I should mention Prof. Alex Rimberg, whose lab space I invaded quite often when doing lithography or evaporation runs, and Prof. Doug Natelson, whose low-temperature epoxy I “borrowed” on more than one occasion. I know that I have not recognized everyone here whose support I appreciated in the course of this project, nor could I if I were ever going to write this thesis.

## Table of Contents

Acknowledgements.....	3
1. Introduction.....	5
1.1 Motivations .....	5
1.2 Background.....	6
1.2.1 Dimensionality .....	6
1.2.2 Fermi surfaces.....	7
2. Antimonide-Based Compound Semiconductors .....	10
2.1 Band Offsets, Band Type, and Bandgap Engineering.....	10
2.2 InAs/AlAs Quantum Well Growth.....	10
3. 2D Magneto-transport Characterization .....	12
3.1 System configuration.....	12
3.2 Sample preparation.....	13
3.2.1 Van der Pauw geometry .....	13
3.2.2 Ohmic contacts.....	13
3.3 Shubnikov-de Haas Measurements.....	14
3.3.1 Landau Indexes and Density Determination.....	15
3.3.3 Measurement Ideality .....	16
3.3.4 Superlattice electron distribution .....	17
4. Cyclotron resonance.....	17
4. Cyclotron resonance.....	18
4.1 Lorentzian Fitting.....	18
5. Electron-beam Lithography .....	20
5.1 Gate Insulation .....	20
5.2 SiO <sub>x</sub> Evaporation and Film Properties .....	21
5.3 Resist Deposition.....	23
5.4 Lithography Exposure.....	23
5.5 Golden gates .....	24
6. Summary.....	26
7. References.....	27

# 1. Introduction

## 1.1 Motivations

The study of nanostructured materials has become the focus of prolific research efforts in recent years. Included in such activities have been both chemical, “top-down” approaches to synthesizing structures with reduced dimensionality, as is the case with carbon nanotubes, and “bottom-up” approaches utilizing, for example, lithographic methods. No matter what the approach, the nanoscale regime makes possible the study of quantum effects with a level of precision unattainable in previous technological eras. One much-touted idea has been to harness the spin degree of freedom for novel devices, suggesting applications in quantum computation and information processing. Such notions, of course, require an extremely thorough understanding of all of the involved physical processes that would contribute to such a spin-based system. Coupling the areas of nanoscale systems with semiconductor physics, already such a fertile area in technological applications, could provide a solid-state realization of such novel device proposals, illuminating many effects of interest in basic physics research along the way.

A number of unique and interesting such effects are already known to arise as the dimensionality of a system is reduced. In an interacting 1D electron picture, for example, theory predicts the transition from a Fermi liquid description to that of the Tomonaga-Luttinger liquid<sup>1</sup>, an entirely new state of matter in which collective modes of spin and charge behave separately—i.e. spin-charge fractionalization. The “0.7 effect” is another, perhaps slightly less exotic, quantum transport phenomenon of interest: as individual energy subbands of a 1D structure become filled, conductance measurements behave as quantized steps of  $0.5 \cdot (G=2e^2/h)$ . Between the lowest such steps, however, an additional feature attributed to an excited many-body state arises at  $0.7 \cdot (2e^2/h)$  and shows a temperature dependence extremely atypical for quantum mechanical systems—that is, the strength of the effect increases with temperature for some range rather than smearing out monotonically with greater thermal energy<sup>2</sup>. Also unique to the 1D realm is the progressive suppression, and hence potential *absence*, of spin relaxation<sup>3</sup>, which would be manifest in optical pump-probe experiments performed on nanowire samples.

By systematically characterizing first the 2D antimonide-based compound semiconductor (ABCS) of interest in the studies presented here, subsequent measurements on 1D ABCS structures will provide a thorough description of how the physical properties of the sample change with decreasing dimensionality. There has been a recent study on 1D channels in this same type of InAs/AlSb heterostructure system<sup>4</sup>, but it addressed only electrical transport measurements, neglecting spin effects entirely. The channel fabrication method was also notably different, employing a selective etching technique instead of a lithographic one using electrostatic depletion of a two-dimensional electron gas (2DEG). This produced a potential profile with harder boundary walls, such that the scattering off the channel edges was specular, but it forgoes the advantage of having an electrostatically defined channel in which the width of the quantum wire is immediately tunable by means of an external applied voltage. Progress on such a lithographic technique as used here is presented in Section 5.

## 1.2 Background

### 1.2.1 Dimensionality

References to “1D” and “2D” structures suggest the need for a working definition of dimensionality. Such a definition, at least qualitatively, derives easily from a simple particle-in-a-box type of picture extended to three dimensions. For example, in a free-particle picture, the dispersion relation of an electron would simply be quadratic,  $E_{\mathbf{k}} = \hbar^2 \mathbf{k}^2 / 2m^*$ , where  $m^*$  is the effective mass in the semiconductor and  $\mathbf{k}^2 = k_x^2 + k_y^2 + k_z^2 = (n_x \pi / l_x)^2 + (n_y \pi / l_y)^2 + (n_z \pi / l_z)^2$  using hard-wall boundary conditions for a 3D box with dimensions  $l_x$ ,  $l_y$ , and  $l_z$ . The longest of the three lengths, say  $l_x$ , would correspond to the widest quantum well, and, hence, the lowest energy level. If a single electron were dumped into the box at  $T=0\text{K}$ , it would then preferentially fill the energy level corresponding to the longest length. Indeed, even at finite temperature, it would still occupy the  $E_x$  level so long as the energy spacing to the next highest level, say  $E_y$ , was larger than the available thermal energy. In other words, the degree of quantum confinement will dictate how the energy levels fill up as more electrons are added into this picture.

The criteria for a “two-dimensional” structure then become a bit clearer: if one length, say  $l_z$ , of the relevant box is much shorter than the other two, then its energy levels will be much higher than those of the unconfined dimensions, and hence remain unpopulated until either such a large number of electrons exist in the system that all the available  $E_x$  and  $E_y$  states are populated or the electrons in those lower-lying levels have enough thermal energy to fill  $z$ -states. Similarly for “one-dimensional” structures, the criteria would be that only  $E_x$  states are filled at some given temperature. In other words, if the Fermi wavelength of the electrons is small compared to one dimension only,  $\lambda_F \ll l_x$ , the expected behavior would be that of a 1D system, whereas if  $\lambda_F \ll l_x, l_y$ , 2D behavior would prevail.

The quantum wells for the studies presented here consist of InAs with AlSb barriers, whose properties are detailed in Section 2. The picture of single energy levels does not completely hold for a regular multiple quantum well structure, or superlattice, as is the case with all of the ABCS samples here. Instead of single, discrete levels, one speaks of energy *subbands*, which indeed are completely analogous.

### 1.2.2 Fermi surfaces

In a simplified picture of a bulk system, energy states may be depicted with a Fermi sphere. For InAs, this is not actually a terribly inaccurate picture, since it is

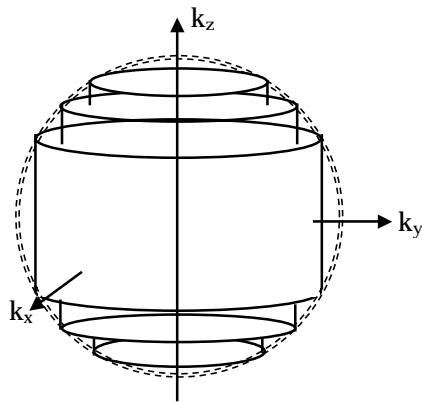


FIGURE 1. Depiction of occupied states in momentum space for a 3D solid in a magnetic field  $B_z$ . Adapted from Ref. [6].

unique in that all its conduction band minima and valence band maxima occur at  $\mathbf{k}=0$ , so the energy surfaces are actually spherical<sup>5</sup>. For  $T=0K$ , all of the states inside the sphere are occupied, and all outside are unoccupied, with electrons near the surface being the exception to this general statement for higher temperatures. Not surprisingly, introducing a magnetic field into this picture has a quantization effect, making the energy levels look like cylinders tangent to the Fermi sphere, as depicted in

Fig. 1. These energy levels satisfy the relation  $E_{nk} = (n + 1/2)\hbar\omega_c + g^* \mu_B B_z + E_z$ , where the first term is the harmonic oscillator-like energy with  $\omega_c = eB/m^*$  being the cyclotron frequency, the second term is the spin magnetic energy, and the third  $E_z = \hbar^2 k_z^2 / 2m^*$  term is the result of any  $z$ -motion of the carriers<sup>6</sup>. Each cylinder, labeled by  $n$  and  $k_z$ , corresponds to a highly degenerate cyclotron, or Landau, level. The radii of the cylinders is described in  $k$ -space as  $k_x^2 + k_y^2 = 2m^*/\hbar^2 (n + 1/2)\hbar\omega_c$ , from which it is evident that increasing the magnetic field strength has the effect of increasing the cyclotron frequency, thereby increasing the radius of the Landau level in momentum space for a given  $n$ . The Fermi energy also increases with the cyclotron frequency,  $E_F = (n + 1/2)\hbar\omega_c$ , such that the number of cylinders inside the Fermi sphere depends on the strength of the magnetic field.

Constricting this into two dimensions means that the Fermi sphere becomes a Fermi disk, looking down from the  $k_z$  axis in Fig. 1. The Landau quantization remains unchanged, but quantum confinement eliminates the  $z$  motion of the carriers. As mentioned, each Landau level is highly degenerate, containing  $eB/\hbar$  number of states—the exact number that would exist between the levels in the absence of a magnetic field. This 2D picture is that of circles entering a Fermi disk (Fig. 2) instead of cylinders entering a sphere, but the qualitative behavior is the same. Thus, whenever a new Landau level enters the Fermi surface, the number of available states in the system—the density of states—diverges, and does so periodically (Fig. 3). As the behavior of the density of states is deterministic of physical properties in general for solid state systems, it is intuitively quite reasonable to expect physical characteristics to oscillate with this quantity. As the Fig. 3 suggests, the DOS goes ideally to zero every period, meaning that there are no available states into which electrons can scatter.

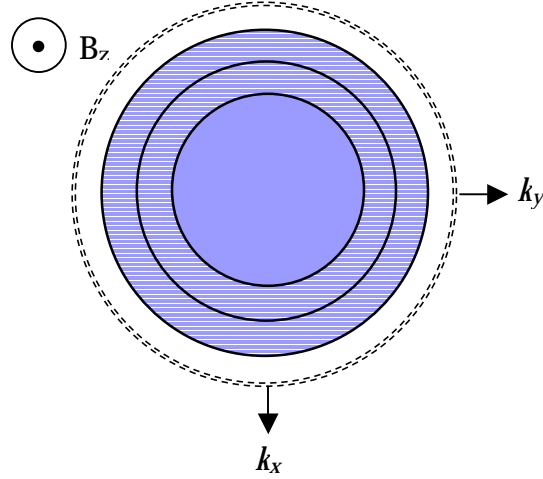


FIGURE 2. Fermi disk for a 2D system. Adapted from Ref. [6].

Likewise, the divergence of the DOS due to a new available Landau level indicates an enormous number of available scattering states. These straightforward observations of the effect of the magnetic field on the DOS of the 2D system play a key role in the interpretation of the magneto-transport measurements described in subsequent sections. The Shubnikov-de Haas measurement is the oscillation of the longitudinal magneto-resistance of the 2DEG sample with magnetic field. Every time a new Landau level enters the system and the DOS diverges, the sudden abundance of available states

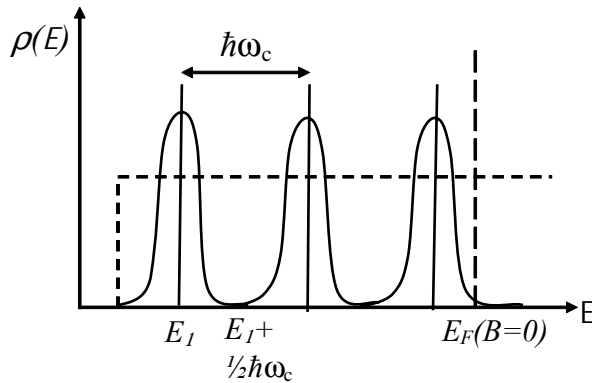


FIGURE 3. Periodic divergence of the density of states, showing broadened Landau levels. Adapted from Ref. [6].

implies an increase in the scattering rate, which implies an increase in the sample resistance. This phenomenon is closely related to the quantum Hall effect, which is a measure of the transverse, rather than longitudinal, magneto-resistance. Instead of oscillations, one observes plateaus in which the

resistance does not change with increasing field strength. The location of these plateaus corresponds to the minima in the longitudinal resistance as measured in the Shubnikov-de Haas technique.

## 2. Antimonide-Based Compound Semiconductors

### 2.1 Band Offsets, Band Type, and Bandgap Engineering

The 6.1-Å family of semiconductors—ABCS including GaSb, InAs, and AlSb—has several unique properties worth describing here. The quantum well materials, InAs and AlSb, have a staggered, type-II band alignment, which means that the valence band

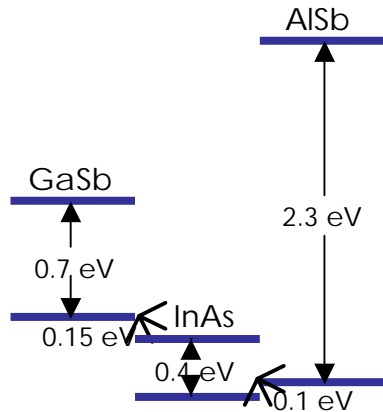


FIGURE 4. Band alignment of 6.1Å semiconductor materials GaSb, InAs, and AlSb.

of one of the materials (AlSb in this case) lies within the bandgap of the other (InAs). Most notably, though, is the enormous conduction band offset of the AlSb, as shown in the band diagram in Fig. 4.

This offset makes ABCS an ideal material to work with for the great flexibility it affords in terms of engineering wavefunctions within the

heterostructures—to which the success of growing quantum cascade lasers with these materials can attest. Also, the Fermi energy for a typical ABCS structure is pinned within the bandgap of the GaSb

cap layer of the heterostructure. Judging by the band diagram alone, it is easy to see that this level must lie in the conduction band of the InAs layers. The GaSb cap layer, therefore, serves as a spatially indirect source of electron donors in the quantum wells. The other primary sources of electrons populating the InAs subbands are the AlSb barriers, although these may be highly growth-dependent.

### 2.2 InAs/AlAs Quantum Well Growth

All of the samples characterized in this study consisted of a InAs/AlSb quantum well structure, grown by molecular beam epitaxy (MBE) at the Osaka Institute of Technology. The sample layers are illustrated in Fig. 5. All of the samples are grown on a GaAs (100) substrate, followed by additional smoothing, buffering layers of AlSb and GaSb that minimize the strain induced by the lattice mismatch between GaAs and the ABCS. After the buffer layers comes a series of twenty identical InAs/AlSb multiple quantum wells, also called a superlattice, which in turn is followed by a 10nm GaSb cap

layer. The only difference from sample to sample is in the InAs quantum wells themselves. The AlSb barrier layers are always 10nm thick, but width of the InAs quantum wells varies from about 3nm to 10nm. Because the GaSb pins the Fermi level but the subband energies for narrower well widths will be higher than those for wider ones, the population of the lowest-energy subbands will vary significantly between samples. Hence, the carrier density in the InAs quantum wells

represents an obvious variable to be determined in characterization measurements. The Shubnikov-de Haas measurements are ideally suited to such density determinations, the data for which are presented in the next section.

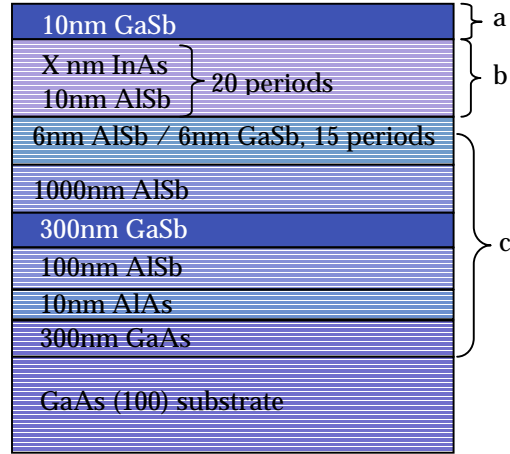


FIGURE 5. ABCS composition layers. a) GaSb cap layer pins  $E_F$ . b) 20-period superlattice of 10nm AlSb alternating with InAs wells of varying width. c) Buffer layers.

### 3. 2D Magneto-transport Characterization

#### 3.1 System configuration

The magnetic fields used in the characterization of the 2DEG ABCS samples are generated in a 10 Tesla superconducting magnet, the Oxford Instruments<sup>7</sup> Spectramag (Fig. 6). The sample lies inside a variable temperature insert (VTI), surrounded by a liquid <sup>4</sup>He reservoir, which is in turn surrounded by a liquid nitrogen jacket.

Adjusting a leak valve, or needle valve, between the helium reservoir and the VTI controls the sample temperature. The sample itself adheres to a copper holder with gold pins inserted into an insulating material using a low-temperature epoxy, as illustrated in Fig. 7, and sits near the bottom of the VTI, at the center of the access windows of the Spectramag. Wires running to the external control circuitry are soldered onto the reverse side of the sample holder as shown in

Figure 7, and run up the length of the magnet stick to 10-pin Fischer connectors which provide easy electronic access to other circuitry control elements. In this case, shielded cables run from the magnet's Fischer connectors to a box with BNC connections built specifically for these transport measurements. Each of the four wires on the sample itself corresponds to a BNC junction on the external box, each of which in turn runs to a lock-in amplifier. The lock-in serves as both the driving current source and the voltage probe. It

outputs a very low-frequency (17 Hz) ac voltage which feeds into a resistive element



FIGURE 6. Oxford Spectramag.

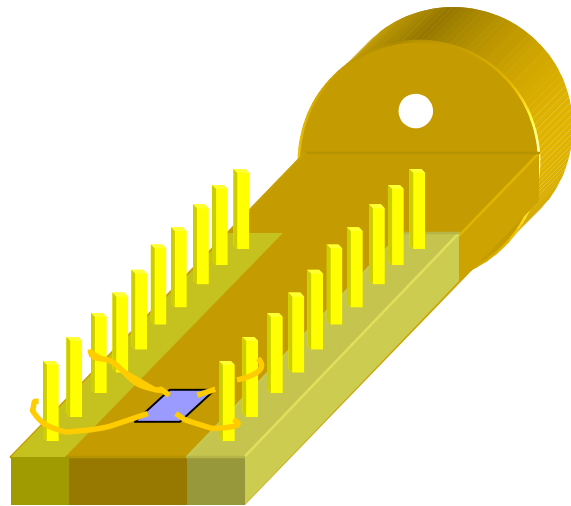


FIGURE 7. Schematic of sample holder with wires bonded to ABCS sample.

inside the BNC box, thereby converting the voltage signal to a current source,  $1\mu\text{A}$  in this case. Thus, two of the connections on the BNC box are used as for the driving current, while the other two measure the voltage response signal.

## 3.2 Sample preparation

### 3.2.1 Van der Pauw geometry

Observation of the classical Hall effect or related quantum effects suggests use of a standard Hall bar on the surface of the semiconductor sample. In such a Hall configuration, a driving current flows through the bar in one direction, while the voltage is measured in the transverse direction—that is, if considering the direction of the applied magnetic field as vertical, the voltage probe is perpendicular to the current flow in the horizontal plane. One known method of avoiding Hall bar fabrication is the Van der Pauw<sup>8</sup> geometry, extremely appealing for its simplicity and practicality. This configuration consists only of four contacts made near the edges of the sample, which in theory may assume any arbitrary shape. The four contacts themselves are arranged in a square. Driving a current through one diagonal of this square while probing the voltage on the other diagonal thus provides a situation in which the measured voltage is perpendicular to the input current, mimicking the geometry of the Hall bar. In order to obtain a quantity independent of the current flow, the measured voltage is generally divided by the current to give a characteristic number with units of resistance, in the Hall case called the transverse resistance or  $R_{xy}$ . In the alternate configuration of the Van der Pauw geometry, current may flow through two contacts on the same side of the square while the voltage reading is off the opposite side. In this case, the resistance value found is the longitudinal resistance, or  $R_{xx}$ . These measurements, as a function of the strength of the applied magnetic field, are frequently employed in studies of two-dimensional electron systems.

### 3.2.2 Ohmic contacts

As with any electronic measurement, the nature of the contact between the sample and probing circuitry plays a crucial role in the accuracy of the measurement. Ohmic behavior describes a contact whose current-voltage characteristic is purely linear,

indicating that electrons are free to flow in either direction across the junction. Non-ohmic behavior may broadly refer to any type of deviation from such linearity; often, for example, an I-V curve will exhibit sub-linear behavior at low current values. This non-ideality may arise from any number of sources, from a native oxide layer acting as an effective tunnel barrier to a choice of contacting material with a greatly differing work function than the material to be measured. This latter case may form an entirely different class of contacts known as Schottky barriers, wherein the mismatch of work functions prevents electrons, even considering thermal energies, from flowing a particular direction. While this type of contact has its uses, Ohmic contacts between the sample 2DEG and the external measurement circuitry are necessary here.

Indium is one appropriate contacting material given the constituent sample layers including GaSb, AlAs, and InAs. Pure indium is also extremely soft, facilitating its manipulation without complicated tools. In the sample preparation process, a fine-tipped soldering iron is used to place four small points of indium onto the corners of the GaSb-capped 2DEG sample. Forming the ohmic contacts with the underlying superlattice requires the indium to diffuse vertically into the sample, a task accomplished with a rapid thermal anneal. This annealing step takes place in an oxygen-free environment in order that the heated metal does not oxidize upon diffusion into the sample and thereby compromise the contact I-V linearity. Typically, a forming gas of either 80% He/20% H<sub>2</sub> or 80% N<sub>2</sub>/20% H<sub>2</sub> is used to this end. Indium has a relatively low melting point for metallic elements, about 157°C, so extremely high temperatures are unnecessary for annealing purposes; for these samples, a five-minute anneal at 210°C proved effective. With the ohmic contacts complete, the connection between the 2DEG sample and external circuitry is made by soldering very fine gold wires from the annealed sample corners to pins on the sample holder.

### 3.3 Shubnikov-de Haas Measurements

Using the Van der Pauw configuration, the measurement of the oscillatory longitudinal electrical resistance with magnetic field, as described in Section 1.2, has become a standard way to characterize 2D electron systems. Indeed, the simplicity in

extracting carrier densities from the raw data traces makes it appealing for determination of such parameters.

### 3.3.1 Landau Indexes and Density Determination

In calculating the density from the data traces, one needs only to look at the spacing of the maxima or minima in a plot of the longitudinal resistance ( $R_{xx}$ ) versus magnetic field. Fig. 8 shows such traces for an ABCS sample with 8.4nm InAs well widths at temperatures of 2K, 10K, and 20K. The Landau index of each peak or valley, when plotted as a function of inverse field strength, is linear, following the particularly

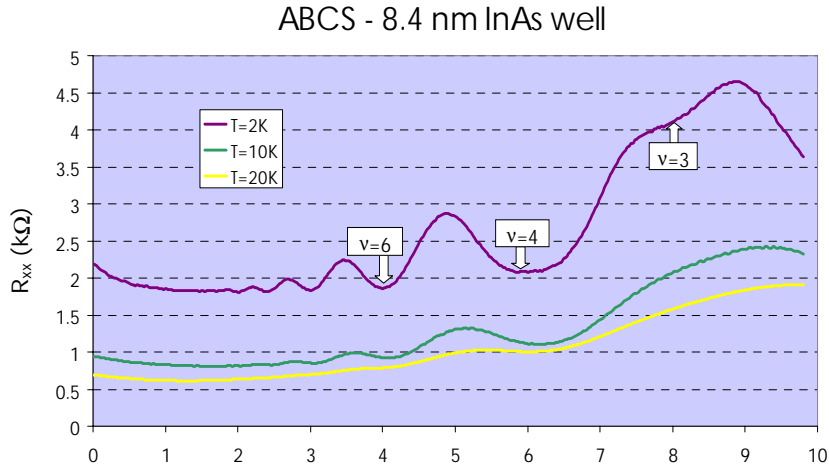


FIGURE 8. Shubnikov-de Haas traces for an 8.4nm well width sample at T=2k, 10K, and 20K.

simple form of  $\nu = \frac{hn_{2D}}{eB}$  where  $\nu$  is the Landau index,  $h$  is Planck's constant,  $n_{2D}$  is the density to be determined, and  $B$  is the magnetic field at the peak or valley of interest. It remains, then, only to determine which Landau number corresponds to which oscillation. Quite generally speaking, higher indexes fall at lower field strengths. Also, the oscillations at lower field strengths are spin-degenerate—that is, both spin species have irresolvable energies. In this spin-degenerate regime, the valleys of the oscillations have even Landau indexes, and the peaks have odd ones. At higher field strengths, this is no longer true; one peak in the Shubnikov-de Haas oscillation will correspond to only spin-up or only spin-down electrons because their energy levels have been sufficiently split by the magnetic field. Evidence of such spin resolution is at 8T for the 1.6K trace

shown in Fig. 8. The easiest method of assigning indexes is to find the highest spin-degenerate peak (valley), then find the peak (valley) at half this field value. For example, the 1.6K trace shown in Fig. 8 exhibits a valley at about  $B=6\text{T}$ , with another valley at about  $B=3\text{T}$ . Because the relationship between the Landau index and inverse field strength is linear, the index of the 3T valley will be exactly twice that of the 6T valley. Counting that there is only one valley between the two, around 4T, and knowing that the valleys of these spin-degenerate oscillations correspond to even numbers uniquely determines the indexes of the 6T and 3T valleys as  $\nu=4$  and  $\nu=8$ , respectively, since these are the only numbers that satisfy one being twice the other with one even number in between, corresponding to the  $\nu=6$  index at 4T.

Having assigned the Landau numbers to individual peaks or valleys of the Shubnikov-de Haas oscillations, determining the density of the quantum well becomes a trivial task using the  $\nu = \frac{hn_{2D}}{eB}$  formula. The Shubnikov-de Haas measurement is sensitive to the per-well density in the structure; since all of the ABCS samples are comprised of a 20-period superlattice, the numbers obtained from that formula need only be multiplied by twenty to yield the total electronic carrier density. For the samples measured, typical densities were on the order of  $\sim 10^{13} \text{ cm}^{-2}$ .

### 3.3.3 Measurement Ideality

The description of Shubnikov-de Haas oscillations as presented in Section 1.2 is rather ideal, suggesting that for any sample the longitudinal resistance should approach zero in every period since there are no available scattering states. In practice, however, as is seen in Fig. 8, the minima are not particularly deep. This owes in part to the cleanness of the samples. Higher mobility samples would also generate cleaner oscillations; for these ABCS samples, mobilities were  $\sim \mu=3000\text{-}5000 \text{ cm}^2/\text{V}\cdot\text{s}$ . For reference, high electron mobility transistors (HEMTs) may have mobilities orders of magnitude greater than this, in the  $15\,000\,000 \text{ cm}^2/\text{V}\cdot\text{s}$  range (Ref. [6]).

Also, large electron densities imply a high Landau index for a given field strength. High Landau levels (occurring at lower fields), though, are more broadened than lower ones (occurring at higher fields), leading to more overlap between adjacent

oscillations. This helps explain why the oscillations at lower field strengths are much less clear, not really even resolvable for the traces shown here until the B field is well above 1 Tesla. The field strengths at when the Shubnikov-de Haas oscillations start to become resolvable is highly sample-dependent, as is the field at which it starts to show spin splitting.

One other source of non-ideality in this type of measurement is the possible mixing of longitudinal and transverse resistivity components. Generally speaking, resistivity is a tensor quantity, with definite relations between the tensor elements (Ref. [6]). Speaking of mixed Shubnikov-de Haas and Hall resistivities is equivalent to saying that the off-diagonal tensor elements are nonzero as they would be in the ideal case. In the Shubnikov-de Haas measurements, such mixing would correspond to more broadened peaks and shallower oscillation minima.

### 3.3.4 Superlattice electron distribution

Electron density is not the only parameter that one can extract from the Shubnikov-de Haas measurements. For example, the variation of effective mass may be determined from the change in oscillation amplitude and peak locations with temperature. Combined with Hall measurements—the other configuration possible with the Van der Pauw geometry—information about the mobility and electron distribution is also available. In this latter case, for example, the Shubnikov-de Haas measurement is sensitive to the average per-well electron density, which then must be multiplied by the number of superlattice periods for a determination of the total carrier density.

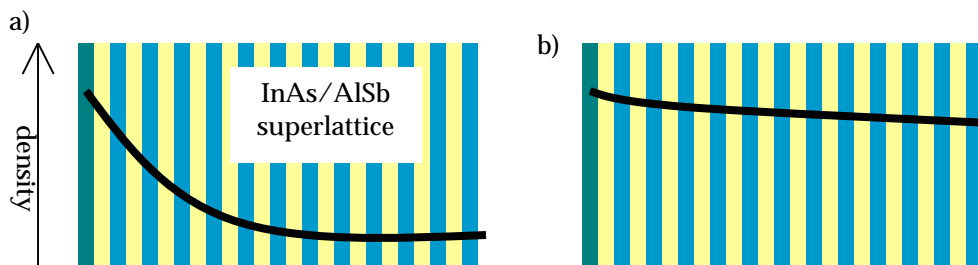


Figure 9. Inferred electron distribution for a)  $20 \cdot \text{SdH density} \gg \text{Hall}$ , b)  $20 \cdot \text{SdH} \sim \text{Hall}$

## 4. Cyclotron resonance

Cyclotron resonance (CR) provides another method of extracting significant information about sample characteristics. Like the Shubnikov-de Haas measurements, this again employs a perpendicular magnetic field, accelerating the carriers in the sample in circular orbits around the field axis. Using a straightforward semi-classical treatment<sup>9</sup> of the electrons in such a field leads to equations of motion, with the resulting angular rotation frequency, or cyclotron frequency,  $\omega_c = \frac{eB}{m^*}$  in SI units. When an external radiation field is introduced parallel to rotation plane, the electronic carriers can resonantly absorb energy from the electric field when its frequency is equal to the cyclotron frequency. Just as the Shubnikov-de Haas oscillation measurements are the preferred method for determining carrier densities, cyclotron resonance is most widely used for determining effective masses.

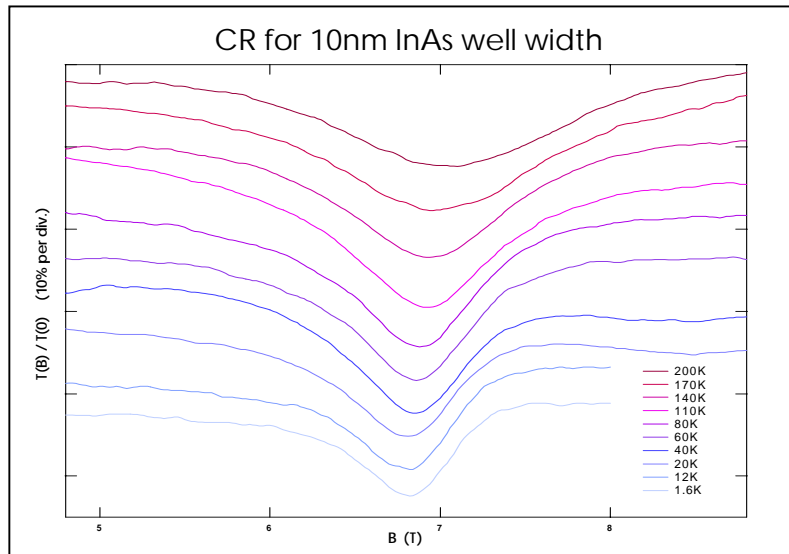
### 4.1 Lorentzian Fitting

The shape of the resonances in a CR experiment correspond to a Lorentzian function of the form  $L = \frac{1}{2c\epsilon_0(\chi_\ell)^{1/2}} \frac{n_s e^2 \tau}{m^*} \frac{1}{1 + (\omega - \omega_c)^2 \tau^2}$ , where  $n$  is the total 2D

density,  $\tau$  is the scattering time,  $m^*$  is the effective mass,  $\omega_c$  is the cyclotron frequency, and  $(\chi_\ell)^{1/2}$  is the real

part of the refractive index of the material, with a value of 3.793 in the case of InAs. IGOR, the software used in the data collection and analysis, can fit the data over a user-defined range to a simplified Lorentzian form, which can then be

converted into the parameters of interest. The effective mass may also be calculated just



from the minima of the resonance position. The figure of merit here is the behavior of the effective mass as a function of temperature. Since the effective mass, is by definition

(Ref. 9) a measure of the band curvature,  $\frac{1}{m^*} = \frac{1}{\hbar^2} \left( \frac{\partial^2 E}{\partial k^2} \right)$ , this provides information

about how temperature affects the band structure of the semiconductor.

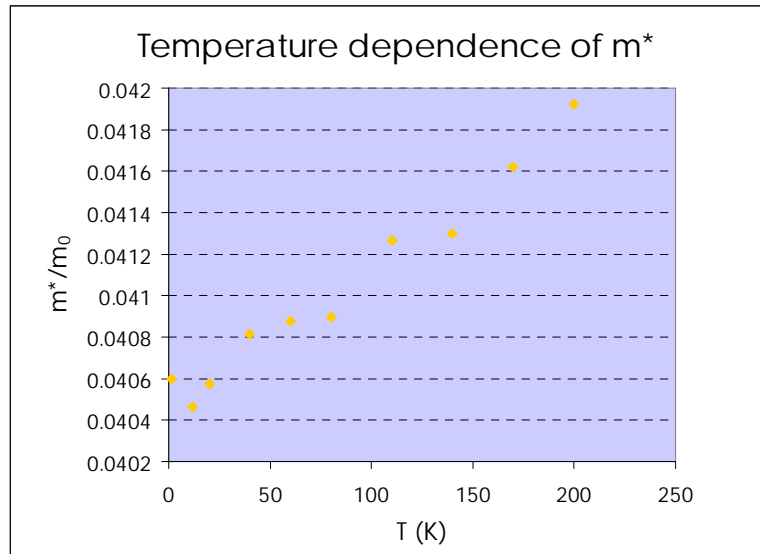


FIGURE 10. Effective mass versus temperature as deduced from cyclotron resonance measurements.

## 5. Electron-beam Lithography

In order to constrain the already quantum-confined electrons in the InAs wells effectively into one dimension, electron-beam lithography is employed. A generic lithography process consists of a few basic steps: deposition of a resist layer, exposure of the resist, and development. The resist used here is polymer called polymethyl methacrylate, or PMMA 950, where the 950 refers to a molecular weight. This is a positive resist convention, meaning that the resist is destroyed upon exposure. The beam of electrons writes the pattern on the resist by breaking the polymer into smaller pieces, such that the areas exposed may wash away more easily than the unexposed portions upon development.

The goal is to define two Schottky gates on the sample surface, separated by only about 100nm. Applying a negative voltage to the split gates locally depletes the underlying semiconductor layers of electrons, such that the electrons in the two-dimensional quantum wells become squeezed into a single channel as determined by the spacing between the metal gates. Indeed, the physical extent of the depletion region continues a length on the order of 50 nm (depending on the applied voltage) laterally beyond the gates themselves, which means that the effective channel width will be smaller than the nominal gate spacing. Preparing the samples for lithographic processing requires a number of preliminary steps, which will be described here.

### 5.1 Gate Insulation

As explained earlier, the GaSb capping layer of all of the sample structures pins the Fermi level of the heterostructure, and thereby serves as one source of electronic carriers in the InAs quantum wells. Avoiding leakage between the metallic gates and this capping layer requires deposition of an additional gate insulator. Such insulation is not necessary in general for split-gate structures, owing rather to the choice of material than the choice of pattern. For this case, the end product will essentially be a metal-insulator-semiconductor (MOS) structure. The gate insulator chosen here is a thermally evaporated silicon monoxide powder. Silicon oxides are widely used among the semiconductor industry for their ease of growth and favorable dielectric properties. In

evaporation of the material, however, additional difficulties arise. Silicon monoxide has a tendency of “spitting” and “spalling”<sup>10</sup> during evaporation, causing pinhole defects in the resulting film. Such a defect would essentially represent a short between the GaSb cap layer and the gates above, avoiding which was precisely the motivation for depositing a



Fig. 11. Example of a baffled box source used in SiO evaporation.

gate insulator in the first place. In effect, the goal is to create a metal-insulator-semiconductor, or MOS structure. To circumvent the difficulties with the silicon monoxide evaporation process, a baffled box source is used, as shown in Fig. 11. Using this type of source eliminates the line of sight between the SiO source and the sample surface, thereby eliminating particulate matter from the vapor stream and reducing the number of defects in the film.

## 5.2 SiO<sub>x</sub> Evaporation and Film Properties<sup>11</sup>

The conditions under which the thermal evaporation takes place play an important role in the properties of the resulting oxide film. The most relevant parameters include the source temperature, the substrate temperature, total pressure, partial pressure of oxygen during the evaporation process. When SiO powder is vaporized at pressures of  $\sim 10^{-4}$  Torr or greater, the resulting films are generally less dense than bulk SiO, porous, and less adherent to the substrate than desired. When the source powder is heated to extremely high temperatures—which is equivalent to having a high evaporation rate—it may disproportionate, leaving small concentrations of free silicon in the deposited film. These patches of silicon strongly absorb in the UV and the blue part of the visible spectrum, resulting in very dark colored films. In terms of electrical properties, though, the films are also characterized by low dielectric strengths and resistivity, unfavorable qualities for insulation purposes.

Introducing pure oxygen into the evaporation chamber greatly modifies the oxidation state of the film, whose composition will then vary between that of pure SiO and pure SiO<sub>2</sub>. Evaporating at very low pressures—less than  $\sim 10^{-5}$  Torr—and fast

evaporation—more than about 60 Å/sec—will produce a film with properties most nearly like pure silicon monoxide, with a dielectric constant  $\kappa \sim 6$  and refractive index  $n \sim 2$  in the visible range. Conversely, higher oxygen partial pressures (and hence, slightly higher total pressures, not to exceed  $10^{-4}$  Torr) and slower evaporation rates result in films more like pure silicon dioxide, with  $\kappa \sim 3.9$  and  $n \sim 1.4$ . In fact, because SiO and SiO<sub>2</sub> films show very characteristic IR absorption at different wavelengths—10 μm for SiO and 9 μm for SiO<sub>2</sub>—measuring the absorption spectra can provide accurate, deterministic information about the oxidation state of the film. For electrical purposes, either type of film will suffice, so long as there is no free silicon present and the film is not porous. For optical measurements, however, as will eventually be performed on the InAs nanowires, the refractive index of the film will prove of particular importance, necessitating highly tailorable, reproducible films. In this sense, oxide film deposition becomes something of a process engineering problem. Currently, the vacuum pressure inside the evaporation chamber is  $\sim 1 \cdot 10^{-6}$  Torr without any oxygen introduced by means of a controlled leak valve. During the evaporation, however, the pressure may increase an entire order of magnitude due to source outgassing and normal vapor pressure of the thermalized SiO powder.

The one parameter previously mentioned that has not been addressed here is the substrate temperature. In the evaporator available, there is no means of independently controlling this temperature. Instead, the box source of SiO acts as a heat source for everything else in the evaporation chamber, whether this is desirable or not. For the substrate, an ideal temperature would be between 473 and 573 K, as in this temperature range there is far less mechanical stress at the substrate cap layer-oxide film interface. This is due to the film annealing on contact to the substrate, and allows for thicker film depositions without a risk of the oxide layer peeling off the substrate shortly after atmospheric exposure. Aside from having no means to control the substrate temperature, there is at this time no means even for its measurement, so the effect of this parameter may be unknown unless extensive modifications to the evaporating system come to pass.

### 5.3 Resist Deposition

Deposition of the e-beam resist—the aforementioned PMMA 950—proves a far easier process than that of the oxide layer. This involves only the use of a standard spinner to apply the resist to the top of the oxide layer. Spin coating the resist at 4500 rpm for 40 seconds provides a very thin, relatively uniform layer of PMMA. In fact, since different thicknesses of the polymer coat will reflect different colors of light, the uniformity of the reflected color can serve as a rough visible gauge of the thickness distribution on the sample chip, which is usually about a 5mm by 5mm square or smaller. The resist layer is then baked on a hot plate at 165°C for 60 minutes to finish the process.

### 5.4 Lithography Exposure

The scanning electron microscope (SEM) used to perform the e-beam lithography here is the LEO 440. In an imaging mode, with no resist considerations, the electron beam may be focused down to a spot size of 2nm. For writing purposes though, the expectation for minimum feature sizes is much greater than the nominal 2nm beam waist, primarily due to a backscattering of electrons in contact with the substrate layers. When the electron beam has penetrated the layer of PMMA resist, the electrons then see only the underlying oxide layer which is insensitive to such exposure. As such, the electrons simply bounce off the oxide and back into the resist layer, forming an undercut of exposed PMMA that washes away upon development of the resist. Clearly then, the reflectivity of the layer underneath the resist—the insulating gate oxide in this case—plays a crucial role in determining the extent of the electron backscattering. This is another reason why the oxide composition and properties must be extremely consistent from sample to sample.

The manner in which the SEM writes a pattern is not continuous: it delivers a set amount of charge for a set amount of time to a point, then stops as the stage moves the sample to the next point, then turns on again to deliver charge to the next point. The strength of the beam in terms of charge delivered per unit area, the spacing of the points where the SEM writes, and the time it spends exposing the given point are collectively referred to as the beam dosage. Determining this dosage is again a problem of process

engineering, with all the pattern parameters controlled by write files at the external computer of the SEM. An optimized beam dosage will provide the minimum feature sizes possible on a given SEM for the particular sample, but due to the undercut of electrons in the resist, that feature size will always be an order of magnitude greater than the nominal 2nm beam waist.

## 5.5 Golden gates

After completion of the pattern exposure, the resist is developed, removing the exposed areas. With the same thermal evaporator as for the oxide, an adhering layer of 2nm chromium is deposited, followed by

18nm of gold. To illustrate the effects of beam dosage optimization, Figs. 12 and 13 show atomic force microscope (AFM) pictures for the cases of underexposure and overexposure, respectively. In the underexposed case, the polymer resist is not broken up sufficiently, so the developer chemical does not rinse it away as completely as it ideally would. This results in pockets of underexposed resist throughout the nominally exposed regions, as is evident in the

micrograph. The resulting channel is extremely rough; trying to use this for electrostatic confinement would generate an extremely irregular potential profile, inducing such a large amount of scattering that no useful transport measurements could

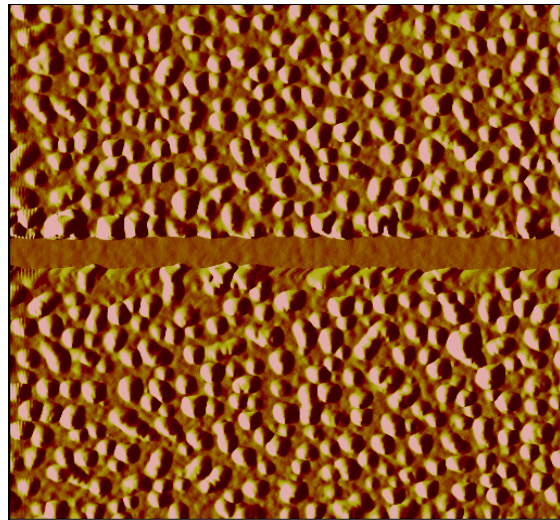


FIGURE 12. AFM image of sample with too little beam dosage. Pockets of undeveloped resist result in channel roughness.

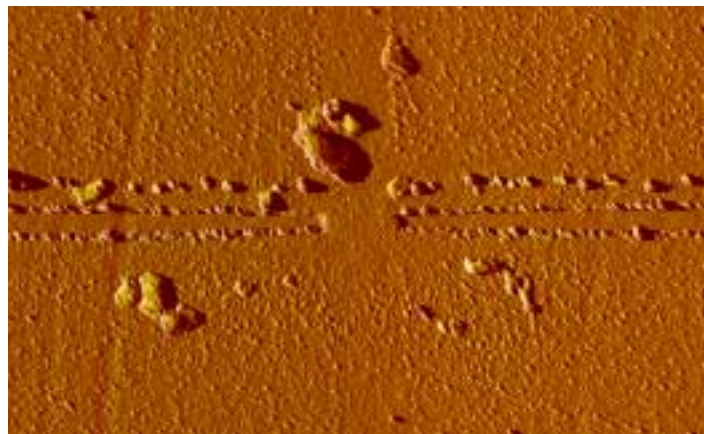


FIGURE 13. AFM image of overdosed sample. Too much electron exposure has pinched off the center of the channel.

be made. On the other extreme, too high a beam dosage can destroy the channel completely by pinching off the center of the pattern. The gate edges for the optimal beam dose would be completely smooth, with about a 100nm separation.

## 6. Summary

The body of work encompassed in the study of the 6.1-Å semiconductor samples thus far by no means represents the end of the investigations. The 2D ABCS heterostructures have been characterized extensively, with even more data reduction possible from the Shubnikov-de Haas and cyclotron resonance measurements performed. In order to systematically study the 1D quantum transport phenomena of interest here, many nanowires must be fabricated for use first in further electrical transport measurements, but also for spin transport which will incorporate an additional optics setup using pump-probe spectroscopy. Much work has been accomplished in terms of process engineering for the lithography optimization, both in terms of oxide reliability and electron beam dosage. The scope of the project has thus reached the point where much discussion can be made about 1D fabrication methods, but has not reached the point where it is possible to speak of 1D characterization.

## 7. References

---

- <sup>1</sup> Voit, J., “One-dimensional Fermi liquids,” Rep. Prog. Phys. **58**, 977 (1995).
- <sup>2</sup> K. J. Thomas, J. T. Nicholls, M. Pepper, W. R. Tribe, M. Y. Simmons, and D. A. Ritchie, Phys. Rev. B **61**, 13 365 (2000).
- <sup>3</sup> A. A. Kiselev and K. W. Kim, Phys. Rev. B. **61**, 13 115 (2000).
- <sup>4</sup> C. Yang, Phys. Rev. B **66** 115306 (2002).
- <sup>5</sup> N. Ashcroft and D. Mermin. *Solid State Physics*. Harcourt (1976).
- <sup>6</sup> Weisbuch and Vinter. *Quantum Semiconductor Structures*. Academic Press (1991).
- <sup>7</sup> Oxford Instruments website, <http://www.oxinst.com/SCNPDP156.htm>
- <sup>8</sup> L.J. Van der Pauw, Philips Res. Repts **13** 1 (1958).
- <sup>9</sup> See, for example, C. Kittel. *Introduction to Solid State Physics*, 7<sup>th</sup> ed. Wiley (1996).
- <sup>10</sup> R.D. Mathis website, <http://www.rdmathis.com>
- <sup>11</sup> See, for example, R. D. Mathis, “Silicon Monoxide – Properties and Evaporation Techniques.”